WING FLUTTER COMPUTATION USING SPECTRAL VOLUME METHOD FOR HYBRID UNSTRUCTURED MESH

Yuta Sawaki[+1], Seiya Tateoka[+2] and Keisuke Sawada[+3]

Tohoku University, Sendai, Japan

Toward accurate prediction of transonic wing flutter phenomenon, an implicit spectral volume method is extended to employ the ALE formulation for moving and deforming grid, and unstructured hybrid meshes for higher computational efficiency. The developed aeroelastic analysis code is applied to compute the transonic flutter of the AGARD 445.6 wing and a rectangular unswept wing. In this study, modal structure analysis is employed. The eigen frequencies and mode shapes of each mode in a reference are employed for the AGARD 445.6 wing flutter analysis. For the rectangular wing flutter analysis, we make the structure plate model using NASTRAN. It is shown that the computed flutter speed index and flutter frequency agree well with the experimental data at subsonic freestream condition, and considering viscous effects improve the computed results in supersonic freestream regime for the AGARD 445.6 wing. In the rectangular flutter case, the flutter speed index at transonic dip cannot be obtained quantitatively. Accounting for viscous effects slightly improve the flutter speed index. On the other hand, the flutter frequency is significantly improved by solving RANS equations at the transonic dip condition compared with that obtained by Euler computation. The cause for this improvement is under consideration.

Keyword: CFD, Unstructured Mesh, Fluid-Structure Interaction

1. INTRODUCTION

Wing flutter is an aeroelastic phenomenon where excitation and deformation of wing become significant due to coupling of aerodynamic, elastic, and inertial forces[1]. Due to the strong demands for environmentally friendly aircrafts, new technologies, such as high-aspect-ratio wings and high-bypass geared turbofan engines are employed to realize low fuel burn, low noise and low emission. These heavier engines may cause flutter in combination with high-aspect-ratio wings because of low bending and torsional stiffness. Because flutter can lead to destruction of wing, accurate aeroelastic analyses of wing flutter are very important for design of recent commercial airplanes which fly through transonic flow regime where dynamic pressure is large.

In numerical analyses of wing flutter, the doublet-lattice method (DLM)[2] coupled with structural code is efficiently employed but it provides poor accuracy in transonic flowfields where shock waves emerge. Use of high fidelity CFD methods in aeroelastic analyses is really desired to take the nonlinear effects into account so far as the computational cost remains acceptable for aircraft design routines.

Arizono et al.[3] conducted experiments and numerical analyses of flutter for wing-pylon-nacelle configuration. They used Euler solver in numerical analyses and rough trends of flutter boundaries are estimated. Morino et al.[4] also calculated flutter for wing-pylon-nacelle configuration using reduced-order model (ROM) compared with full-order inviscid CFD. These researches show the two types of flutter trend for wing-pylon-nacelle configuration; mild flutter (hump mode) observed in transonic regime including transonic dip and hard flutter observed in high Mach number. These trends should be accurately predicted for real aircraft development, so higher spatial accuracy and geometrical flexibility are important for flutter computations around such complicated real configuration. Unstructured CFD methods surely provide geometrical flexibility, but generally their spatial accuracy seems insufficient.

In a couple of decades, a lot of high-order unstructured mesh methods are developed and improved.

[+1]sawaki@cfd.mech.tohoku.ac.jp, [+2]tateoka@cfd.mech.tohoku.ac.jp, [+3]sawada@cfd.mech.tohoku.ac.jp

Discontinuous Galerkin (DG) method[5] is the most widely used high-order numerical method employing finite element discretization. Spectral Volume (SV) method[6] is based on the idea of subdividing each computational cell into sub-cells employing finite volume discretization. Flux Reconstruction (FR) method[7] is the latest high-order numerical method amounts to evaluating the straightforward derivative of a piecewise polynomial with correction at the cell interface employing finite difference discretization. In this study, we employ SV method because hierarchical cell structure can be utilized for *h*-adaptive strategy and sub-cell-based shock capturing[8]. In flutter analyses, the level of flutter boundary and transonic dip depends on the shock wave location, so numerically capturing the shock wave has great significance. In the conventional SV method, for a second-order of spatial accuracy, as many as four degrees of freedom (DOFs) are introduced into a tetrahedral cell to reconstruct a linear polynomial of dependent variables. A tetrahedral cell volume is divided into four sub-cells and the conservative variables in these sub-cells correspond the DOFs. The time evolution of these DOFs in each cell is computed. For high Reynolds number flowfields, thin boundary layer needs to be resolved. In order to reduce the number of computational cells and also to retain the spatial accuracy of the conventional finite volume methods, it is customary to employ prismatic cell layers on the solid wall. Although the spatial accuracy of the second-order SV method is strictly retained even for skewed tetrahedral computational cells, we proposed to formulate the SV discretization for prismatic computational cells to reduce the total number of computational cells in the boundary layer region[9]. Moreover, in flutter analyses, we need to compute flowfields using moving and deforming meshes. The arbitrary Lagrangian-Eulerian (ALE) method solving the geometric conservation law (GCL)[10] is implemented in the present SV code.

   In section 2, the details of the present aeroelastic analysis code based on the spectral volume discretization is described. In section 3, the computed results using the developed aeroelastic code are shown for the AGARD 445.6 wing flutter and the rectangular wing flutter. Finally we summarize the present study in section 4.

2. NUMERICAL METHOD
(1) Arbitrary Lagrangian-Eulerian (ALE) form
The unsteady, three-dimensional, compressible Navier-Stokes equations in the conservative form can be expressed as

$$\frac{\partial \boldsymbol{Q}}{\partial t} + \nabla \cdot \boldsymbol{F}(\boldsymbol{Q}) - \nabla \cdot \boldsymbol{F}_{\mathbf{v}}(\boldsymbol{Q}, \nabla \boldsymbol{Q}) = 0, \tag{1}$$

where $\boldsymbol{Q}$ represents the vector of conservative variables, $\boldsymbol{F}$ the vectors of inviscid fluxes, and $\boldsymbol{F}_{\mathbf{v}}$ the vectors of viscous fluxes. Integration of Eq. 1 over a moving and deforming control volume $\Omega(t)$ yields

$$\int_{\Omega} \frac{\partial \boldsymbol{Q}}{\partial t} dV + \int_{\partial \Omega} (\boldsymbol{F} - \boldsymbol{F}_{\mathbf{v}}) \cdot \boldsymbol{n} dS = 0. \tag{2}$$

Applying the differential identity to the time derivative term gives

$$\frac{\partial}{\partial t} \int_{\Omega} \boldsymbol{Q} \, dV = \int_{\Omega} \frac{\partial \boldsymbol{Q}}{\partial t} dV + \int_{\partial \Omega} \boldsymbol{Q} \{ \dot{\boldsymbol{x}} \cdot \boldsymbol{n} \} dS, \tag{3}$$

where $\dot{\boldsymbol{x}}$ and $\boldsymbol{n}$ denote the grid velocity and the unit normal vector of the surface, respectively. Substituting Eq. 3 into Eq. 2, we obtain

$$\frac{\partial}{\partial t} \int_{\Omega} \boldsymbol{Q} \, dV + \int_{\partial \Omega} (\boldsymbol{F} - \boldsymbol{F}_{\mathbf{v}} - \boldsymbol{Q} \dot{\boldsymbol{x}}) \cdot \boldsymbol{n} \, dS = 0. \tag{4}$$

Assuming that $\overline{\boldsymbol{Q}}$ represents the cell-averaged values, Eq. 4 becomes

$$\frac{\partial}{\partial t} (V \overline{\boldsymbol{Q}}) = - \int_{\partial \Omega} (\boldsymbol{F} - \boldsymbol{F}_{\mathbf{v}} - \boldsymbol{Q} \dot{\boldsymbol{x}}) \cdot \boldsymbol{n} \, dS, \tag{5}$$

$$\frac{\partial \overline{\boldsymbol{Q}}}{\partial t} V + \frac{\partial V}{\partial t} \overline{\boldsymbol{Q}} = -\int_{\partial \Omega} (\boldsymbol{F} - \boldsymbol{F}_{\mathrm{v}} - \boldsymbol{Q}\dot{\boldsymbol{x}}) \cdot \boldsymbol{n} \, dS, \tag{6}$$

$$\frac{\partial \overline{\boldsymbol{Q}}}{\partial t} + \frac{\partial V}{\partial t} \frac{\overline{\boldsymbol{Q}}}{V} = \boldsymbol{R}, \tag{7}$$

where we define the residual operator

$$\boldsymbol{R} = -\frac{1}{V} \int_{\partial \Omega} (\boldsymbol{F} - \boldsymbol{F}_{\mathrm{v}} - \boldsymbol{Q}\dot{\boldsymbol{x}}) \cdot \boldsymbol{n} \, dS \tag{8}$$

for convenience.

(2) Geometric Conservation Law (GCL)

Assuming that $\boldsymbol{Q}$ is constant over the entire domain, we obtain

$$\frac{\partial V}{\partial t} = \int_{\partial \Omega} (\dot{\boldsymbol{x}} \cdot \boldsymbol{n}) \, dS. \tag{9}$$

This relation indicates the geometric conservation law[10] in which the time derivative of cell volume is coincides with the surface integral of projected grid velocity. In the finite volume discretization, in order to satisfy Eq. 9, the projected grid velocity at each cell interface is evaluated by

$$\dot{\boldsymbol{x}} \cdot \boldsymbol{n} = \left(\frac{\partial V}{\partial t}\right)/S, \tag{10}$$

where S represents the area of cell interface and $\partial V/\partial t$ the volume extruded by the surface in Δt.

(3) Spectral volume formulation

In the SV method, a computational cell referred to as the SV cell is partitioned into a set of sub-cells referred to as the control volume (CV) cells. The conservative variables in these CV cells correspond to the degrees of freedom (DOFs) in the spectral volume formulation. When a second-order scheme is considered, four CV cells in a tetrahedral cell[11] and six CV cells in a prismatic cell[9] are used to reconstruct a linear distribution of the dependent variables in a SV cell. The partitions of the tetrahedral cell and prismatic cell are shown in Fig. 1. Let us denote the CV cell-averaged conservative variables in j-th CV cell within a SV cell as $\overline{\boldsymbol{Q}}_j$. The reconstructed variables in an arbitrary location within a SV cell can be expressed by

$$\boldsymbol{Q}(\vec{r}, t) = \sum_{j=1}^{N} L_j(\xi, \eta, \zeta) \, \overline{\boldsymbol{Q}}_j(t), \tag{11}$$

where L_j denotes the shape function for j-th CV cell, and N the number of CV cells in each SV cell. This shape function satisfies the following orthogonal relations

$$\frac{1}{V_j} \int_{\mathrm{CV}_j} L_k(\xi, \eta, \zeta) dV = \delta_{j,k} \quad (j, k = 1, \dots, N), \tag{12}$$

where $\delta_{j,k}$ represents the Kronecker's delta function. Because $\boldsymbol{Q}$ in Eq. 11 are cell-wise polynomials, they become discontinuous at the SV cell interface. The numerical flux functions at the cell interface are determined by an approximate Riemann solver. In this study, we employ SLAU scheme[12] which is one of the AUSM-family. When the computational meshes are moving and deforming, a modified SLAU scheme[13] taking the grid velocity into account is utilized. Viscous flux functions are computed using BR2 formulation by Bassi and Rebay[14]. Flux functions at the interface of two adjacent CV cells inside a SV cell are analytically obtained because reconstructed variables are continuous there.
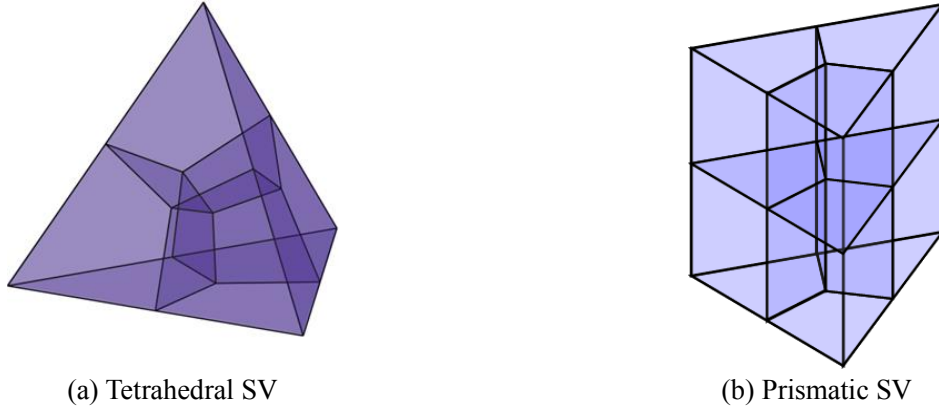
(a) Tetrahedral SV   (b) Prismatic SV
Figure 1: Partitions of tetrahedral and prismatic SV cells.

(4) LU-SGS implicit method

The lower-upper symmetric Gauss-Seidel (LU-SGS) implicit method[15] is employed in the time integration. From Eq. 7, the first-order fully implicit scheme is expressed as

$$\frac{\overline{\boldsymbol{Q}}_c^{n+1} - \overline{\boldsymbol{Q}}_c^n}{\Delta t} + \frac{V^{n+1} - V^n}{\Delta t}\frac{\overline{\boldsymbol{Q}}_c^{n+1}}{V^{n+1}} = \boldsymbol{R}_c(\overline{\boldsymbol{Q}}^{n+1}), \tag{13}$$

where the subscript c denotes the current SV cell. In Eq. 13, $\partial V/\partial t$ is evaluated in first-order. We note that the number of components of vectors $\overline{\boldsymbol{Q}}_c$ and $\boldsymbol{R}_c$ is given as the product of the number of dependent variables and the number of DOFs in a SV. Because $\boldsymbol{R}_c$ depends not only on $\overline{\boldsymbol{Q}}_c$ but also on $\overline{\boldsymbol{Q}}_{nb}$ in the neighbor cells through the numerical fluxes, a linearization of the residual yields

$$\boldsymbol{R}_c(\overline{\boldsymbol{Q}}^{n+1}) \approx \boldsymbol{R}_c(\overline{\boldsymbol{Q}}^n) + \frac{\partial \boldsymbol{R}_c}{\partial \overline{\boldsymbol{Q}}_c}\Delta\overline{\boldsymbol{Q}}_c + \sum_{nb \neq c}\frac{\partial \boldsymbol{R}_c}{\partial \overline{\boldsymbol{Q}}_{nb}}\Delta\overline{\boldsymbol{Q}}_{nb}. \tag{14}$$

Substituting Eq. 14 into Eq. 13 gives

$$\left(\dot{V}_{ratio} + \frac{I}{\Delta t} - \frac{\partial \boldsymbol{R}_c}{\partial \overline{\boldsymbol{Q}}_c}\right)\Delta\overline{\boldsymbol{Q}}_c - \sum_{nb \neq c}\frac{\partial \boldsymbol{R}_c}{\partial \overline{\boldsymbol{Q}}_{nb}}\Delta\overline{\boldsymbol{Q}}_{nb} = \boldsymbol{R}_c(\overline{\boldsymbol{Q}}^n) - \dot{V}_{ratio}\overline{\boldsymbol{Q}}_c^n, \tag{15}$$

where $\dot{V}_{ratio}$ denotes the ratio of time derivative of cell volume $\partial V/\partial t$ to the latest cell volume. In order to avoid storing the Jacobian matrices for the "nb" cells, inner iterations are further introduced. Equation 13 can be rewritten using inner sweep number k as

$$\frac{\overline{\boldsymbol{Q}}_c^{k+1} - \overline{\boldsymbol{Q}}_c^k}{\Delta t} + \frac{V^{k+1} - V^k}{\Delta t}\frac{\overline{\boldsymbol{Q}}_c^{k+1}}{V^{k+1}} = \boldsymbol{R}_c(\overline{\boldsymbol{Q}}^{k+1}). \tag{16}$$

Linearization of the residual in terms of the current cell yields

$$\boldsymbol{R}_c(\overline{\boldsymbol{Q}}^{k+1}) = \boldsymbol{R}_c(\overline{\boldsymbol{Q}}_c^{k+1}, \overline{\boldsymbol{Q}}_{nb}^{k+1}) \approx \boldsymbol{R}_c(\overline{\boldsymbol{Q}}_c^k, \overline{\boldsymbol{Q}}_{nb}^{k+1}) + \frac{\partial \boldsymbol{R}_c}{\partial \overline{\boldsymbol{Q}}_c}(\overline{\boldsymbol{Q}}_c^{k+1} - \overline{\boldsymbol{Q}}_c^k). \tag{17}$$

Substituting Eq. 17 into Eq. 16, we obtain

$$\left(\dot{V}_{ratio} + \frac{I}{\Delta t} - \frac{\partial \boldsymbol{R}_c}{\partial \overline{\boldsymbol{Q}}_c}\right)(\overline{\boldsymbol{Q}}_c^{k+1} - \overline{\boldsymbol{Q}}_c^k) = \boldsymbol{R}_c(\overline{\boldsymbol{Q}}_c^k, \overline{\boldsymbol{Q}}_{nb}^{k+1}) - \frac{\overline{\boldsymbol{Q}}_c^k - \overline{\boldsymbol{Q}}_c^n}{\Delta t} - \dot{V}_{ratio}\overline{\boldsymbol{Q}}_c^n$$

$$\approx \boldsymbol{R}_c(\overline{\boldsymbol{Q}}_c^k, \overline{\boldsymbol{Q}}_{nb}^*) - \frac{\overline{\boldsymbol{Q}}_c^k - \overline{\boldsymbol{Q}}_c^n}{\Delta t} - \dot{V}_{ratio}\overline{\boldsymbol{Q}}_c^n, \tag{18}$$

in which we replace $\overline{\boldsymbol{Q}}_{nb}^{k+1}$ by the latest solution $\overline{\boldsymbol{Q}}_{nb}^*$ in the neighbor cells. The solutions are updated with multiple symmetric forward and backward sweeps in the domain. If a higher-order time accuracy is needed, the second-order backward difference formula (BDF2) is employed to evaluate $\partial Q/\partial t$ and $\partial V/\partial t$.

3. FLUTTER ANALYSES AND DISCUSSIONS

(1) AGARD 445.6 wing

The AGARD 445.6 weakened model flutter cases are computed using the developed aeroelastic SV code accounting for hybrid unstructured meshes and fluid-structure interaction. A tightly coupling method is employed in which the temporal evolution of the flowfield and structural deformation of the wing are alternately solved with several inner iterations within one time step. The computational conditions follow those of experiment described by Yates[16]. The angle of attack is 0 [deg]. The freestream Mach numbers are 0.499, 0.678, 0.901, 0.960, 1.072, and 1.141. The Reynolds number based on the mean aerodynamic chord (MAC) length is about one million. The structure model of Yates[16] having 10×10 elements shown in Fig. 2 is used in which three bending modes and two twisting modes of the wing are considered in the modal analysis. This model is a plate model. The eigen frequencies of this model are summarized in Tab. 1. In the structural calculation, the eigen frequencies of each modes and modal shape data at all grid points of each modes are needed.
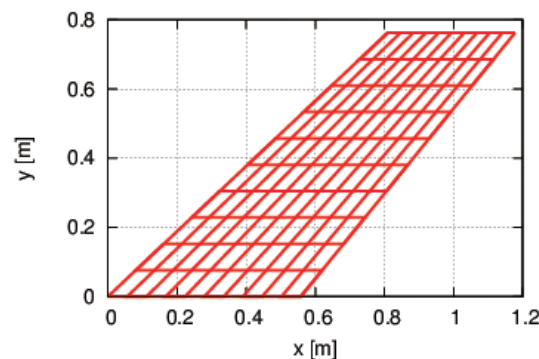

Figure 2: Structure model for the AGARD 445.6 wing by Yates[16].
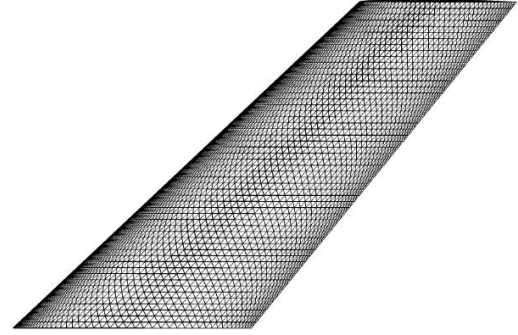
Table 1: Eigen frequencies used in calculations and experimental data for the AGARD 445.6 wing.

Mode		1st (Bending)	2nd (Torsion)	3rd (Bending)	4th (Torsion)	5th (Bending)
Eigen frequency [Hz]	Yates's model[16]	9.6	38.2	48.3	91.5	118.1
	Experiment	9.6	38.1	50.7	98.5	–

The computational surface meshes are shown in Fig. 3. In the Euler computation, 193,068 tetrahedral cells are used. In the RANS calculation, 178,278 tetrahedral cells and 310,464 prismatic cells (24 layers) are employed in which the minimum grid spacing on the wall satisfies $y^+ \leq 2$ for all flow conditions. The Spalart-Allmaras turbulence model[17] (SA noft2) is used in the RANS computation. The outer boundary of the computational domain is located at 30 MAC length from the wing surface. In the present aeroelastic calculations, the computational mesh moves and deform according to the structure displacement. Mesh deformation at each iteration is accomplished by using interpolation method utilizing the inverse distance weighting function. In the implicit time integration, the BDF2 is employed. The inner iterations are continued till the L1 norm of density computed by using all residuals in the entire domain less than 10^{-7}. The number of inner iterations is typically eight when Δt is 0.005 in the Euler computation. In the RANS computation, the number of inner iterations is less than 30 for Δt of 0.05. The unsteady flow calculation starts from the steady flowfield solution with a small oscillation enforced in the first bending mode.
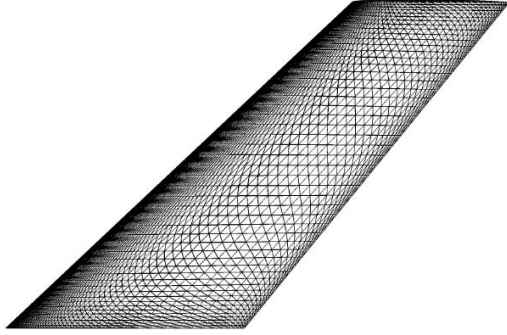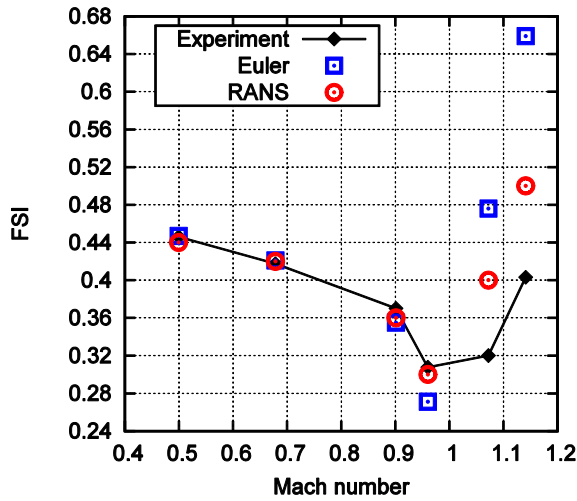
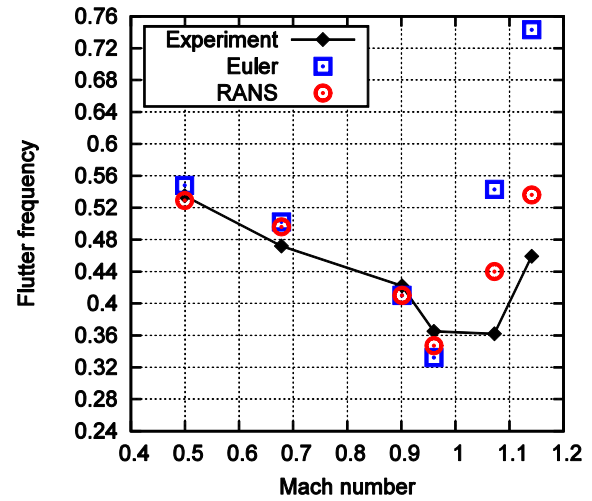(a) Mesh for Euler computations   (b) Mesh for RANS computations
Figure 3: Computational surface meshes for the AGARD 445.6 wing.

(a) Flutter speed index   (b) Flutter frequency
Figure 4: Flutter boundary values for the AGARD 445.6 wing.

The flutter boundaries computed in this study are shown with experimental data in Fig. 4. The horizontal axis represents the freestream Mach number and the vertical axis the flutter speed index (FSI) in Fig. 4(a), and the flutter frequency in Fig. 4(b), respectively. The FSI is expressed by

$$FSI = \frac{U_\infty}{b_s \omega_a \sqrt{\mu}}, \tag{19}$$

where U_∞ denotes the freestream velocity, b_s the half root chord length, ω_a the eigen angular frequency of the first torsion, and μ the fluid-to-structure mass ratio. The flutter frequency is expressed by ω/ω_a where ω denotes the frequency at the flutter boundary point. The calculated flutter boundary shows good agreements with experimental data in the Euler computation as well as the RANS computation so far as the

freestream is subsonic and no shock wave appears on the wing surface. The "transonic dip" is successfully obtained in which the shock wave appears. However, some distinctions between the computed flutter boundary values and those of experiment become evident at supersonic freestream conditions. We note that results in RANS computations give closer agreements with experimental data than those in Euler computations. This implies that the distinctions seen in the supersonic freestream cases are caused by possible shock boundary layer interaction near the trailing edge, which the Euler calculation cannot account for. The pressure coefficient contours obtained by steady inviscid simulations are plotted on the wing surface as shown in Fig. 5.

(a) $M_\infty = 0.499$

(b) $M_\infty = 0.678$

(c) $M_\infty = 0.901$

(d) $M_\infty = 0.960$

(e) $M_\infty = 1.072$
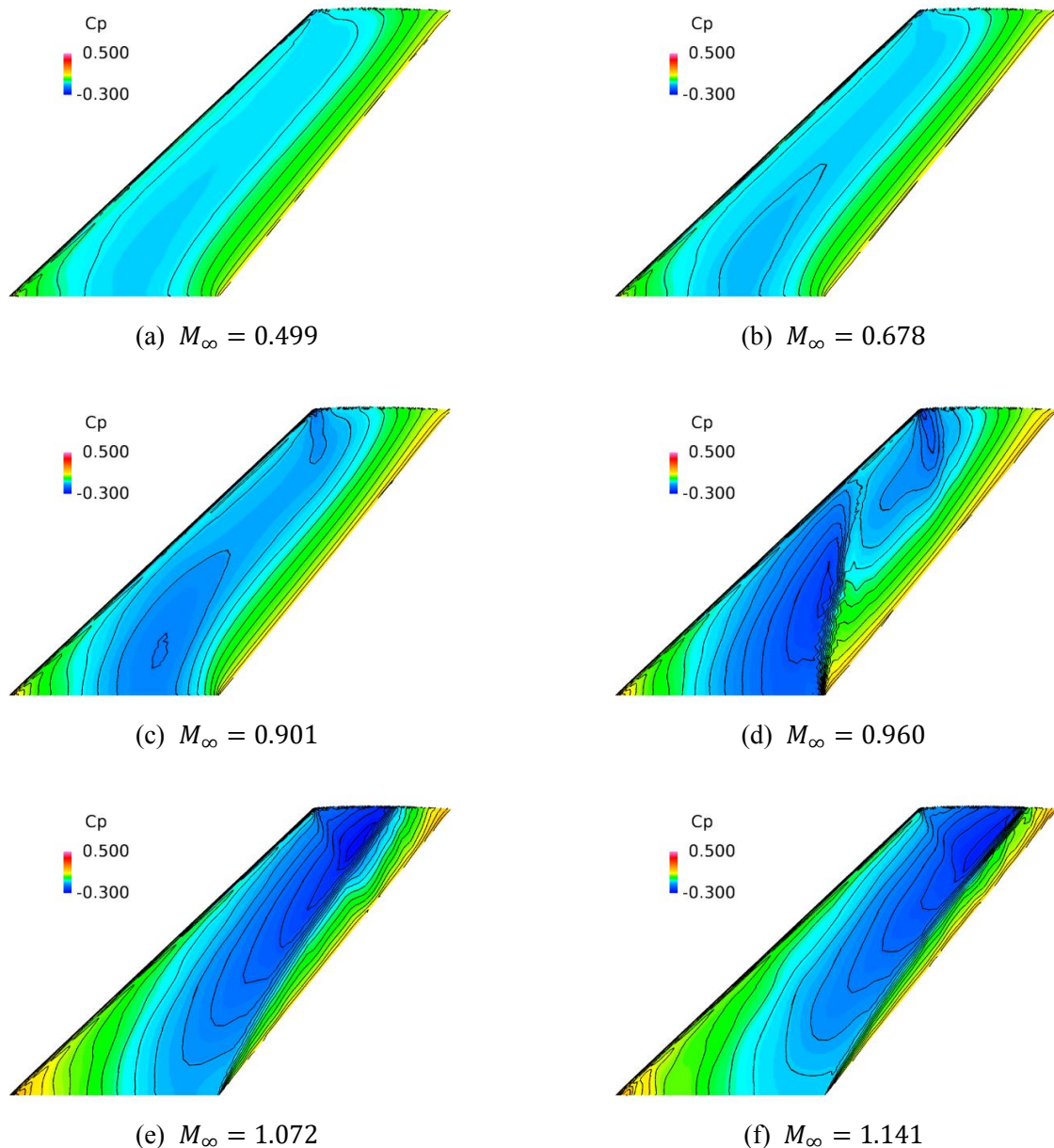
(f) $M_\infty = 1.141$

Figure 5: Pressure coefficient contours for steady inviscid flowfields over the AGARD 445.6 wing.

When the freestream Mach number becomes 0.96 or higher, a strong shock wave appears on the wing which moves toward the trailing edge as the freestream Mach number increases. The pressure coefficients at several spanwise cross-sections computed by both the Euler and the RANS calculations are plotted in Fig. 6. The difference in C_p distribution between these simulations becomes apparent when a shock wave emerges in the

freestream Mach number above 0.96 where significant shock boundary layer interaction begins to take place. Indeed, the pressure coefficients show smooth profiles at the shock location when viscous effects are taken into account in the simulation.
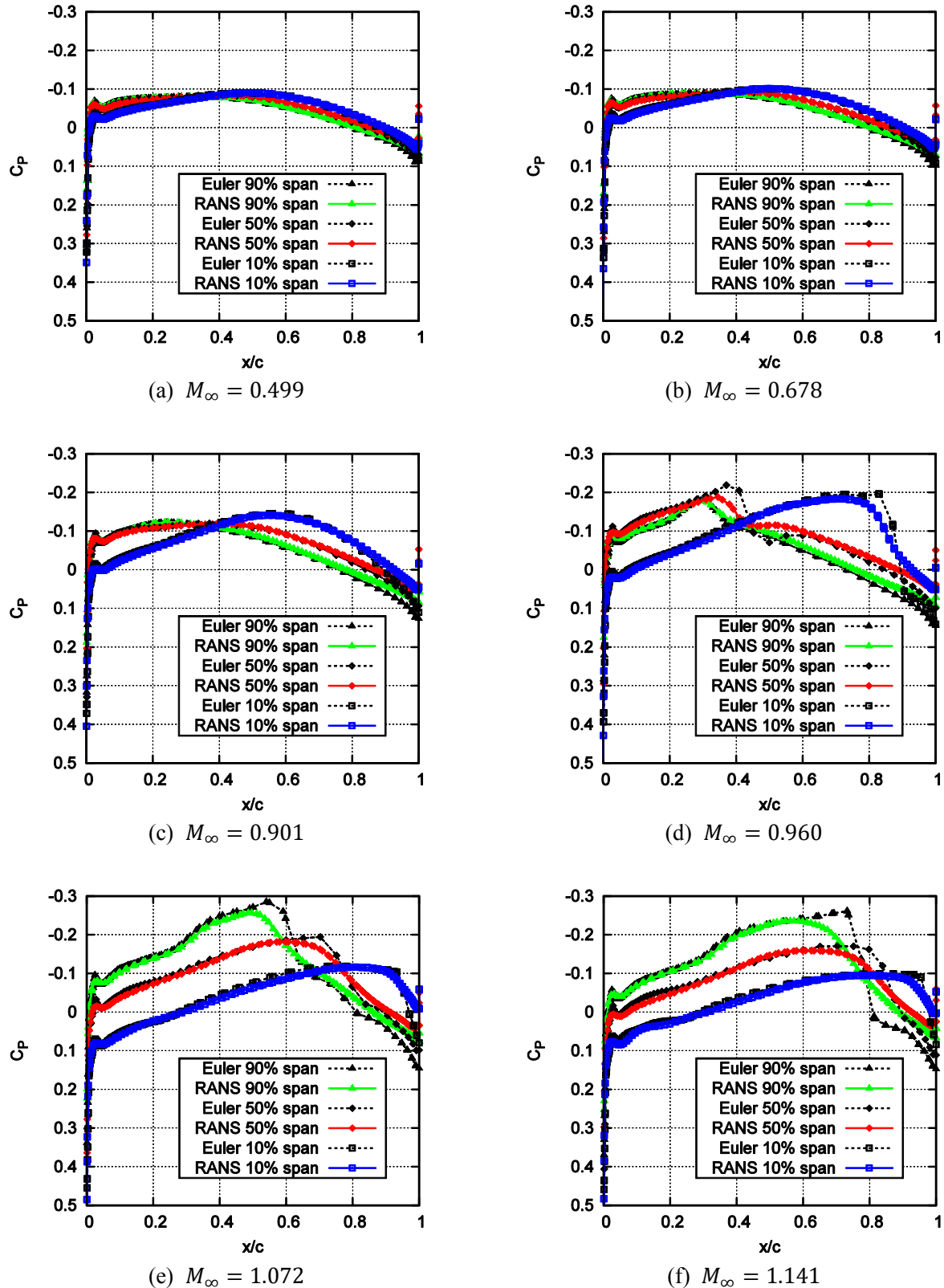

(a) $M_\infty = 0.499$

(b) $M_\infty = 0.678$

(c) $M_\infty = 0.901$

(d) $M_\infty = 0.960$

(e) $M_\infty = 1.072$

(f) $M_\infty = 1.141$

Figure 6: Pressure coefficients at several spanwise cross-sections over the AGARD 445.6 wing.

Gan et al.[18] used delayed detached eddy simulation (DDES) on structured meshes for supersonic cases of the AGARD 445.6 wing flutter and computed flutter boundaries show excellent agreements with experimental data even for supersonic freestream regime. For better agreements with experiment, it seems to be necessary to resolve accurately the shock boundary layer interaction in high Mach number condition. In order to investigate effects of the grid resolution in this study, the coarse mesh and fine mesh are prepared as shown in Fig. 7. The coarse mesh is same as the mesh in Fig. 3 (b). In the fine mesh, grids near the shock wave on the wing surface are refined, and wall-normal grid distribution is same as the coarse mesh. Figure 8 shows the corresponding computed C_L histories. These cases on the coarse mesh and the fine mesh are computed using the SA model in the Mach number of 1.141 and *FSI* of 0.45 above the experimental flutter point. The history employing the fine mesh shows slightly improved trend of oscillation but an expected flutter boundary point will be still higher than that of experiment.

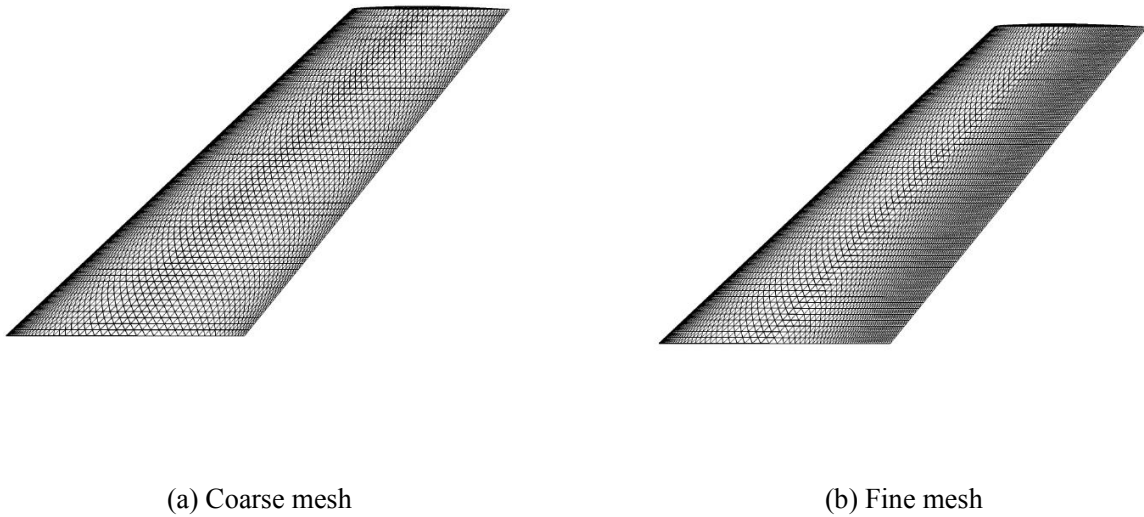| (a) Coarse mesh | (b) Fine mesh |

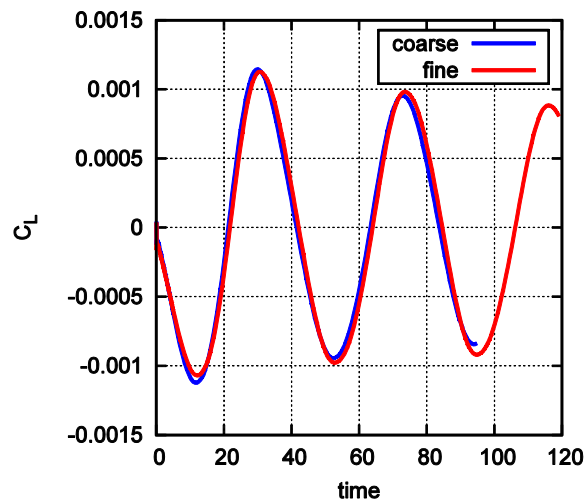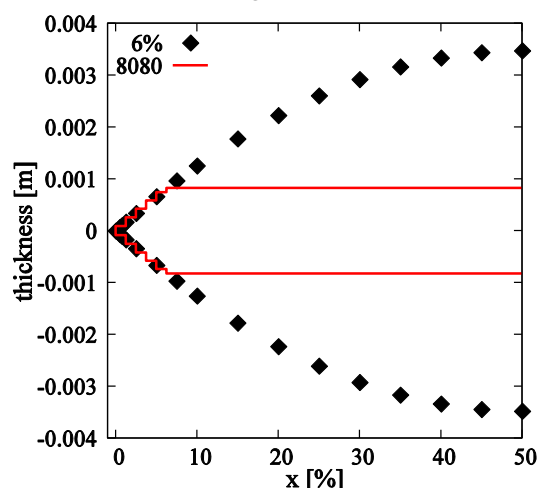Figure 7: Computational surface meshes in RANS computations for the AGARD 445.6 wing.

Figure 8: C_L histories using the coarse mesh and the fine mesh in $M_\infty = 1.141$ and *FSI* =0.45.

(2) Rectangular wing

In the second flutter analysis case, a wing having a rectangular and unswept plan form with a circular-arc airfoil section is employed. This wing has a 6% thickness to the chord length, taper ratio of 1, and aspect ratio of 2.5. The computational conditions follow those of experiment described by Doggett et al.[19] The angle of attack is 0 [deg]. The freestream Mach numbers are 0.715, 0.814, 0.851, 0.913, 0.956, and 1.017. The Reynolds number based on the MAC length is about one million. In these cases, we make a structure model using Femap with NX NASTRAN. In the experiment, a 0.065-inch-thick aluminum alloy plate of the desired plan form was covered with a lightweight flexible plastic foam to make a circular-arc airfoil section. In the reference[19], it is noted that the foam added comparatively little mass and stiffness to that of the aluminum alloy. Therefore, we regard effects of the foam as negligible, and only aluminum core plate is modeled. The plate model has 80×80 elements is shown in Fig. 9. As shown in Fig. 9 (b), thickness of elements at the leading edge and the trailing edge is adjusted in tune with the circular-arc airfoil section. In this model, three bending modes and two twisting modes of the wing are considered in the modal analysis. The eigen frequencies of this model are summarized in Tab. 2. It is confirmed that 80×80 elements is enough number in terms of frequencies of each modes by comparing with other models having different number of elements.
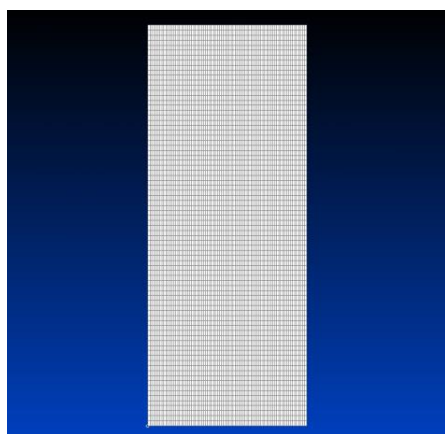
(a) Wing surface of 80×80 plate model   (b) Cross-section

Figure 9: Structure model for the rectangular wing.

Table 2: Eigen frequencies used in flutter computations for the rectangular wing.

Mode		1st (Bending)	2nd (Torsion)	3rd (Bending)	4th (Torsion)	5th (Bending)
Eigen frequency [Hz]	Present model	14.35	77.75	89.34	246.4	250.6
	Experiment	14.29	80.41	89.80	–	–

The computational surface mesh which is same in both Euler and RANS mesh is shown in Fig. 10. In the Euler computation, 209,534 tetrahedral cells are used. In the RANS calculation, 369,878 tetrahedral cells and 252,540 prismatic cells (24 layers) are employed in which the minimum grid spacing on the wall satisfies $y^+ \leq 1$ for all flow conditions. The outer boundary of the computational domain is located at 30 MAC length from the wing surface.

The computed flutter boundaries are shown with experimental data in Fig. 11. When the freestream Mach number is less than 0.913, good agreements with experiment are obtained in both the *FSI* and the flutter frequency. However, the computed *FSI* values are overestimated in high Mach number regime where the shock wave emerges. Considering viscous effects did not improve significantly the *FSI* boundary values. On the other hand, the flutter frequency values at the $M_\infty = 0.913$ is particularly improved by accounting for viscous effects. The cause for this improvement is under consideration.
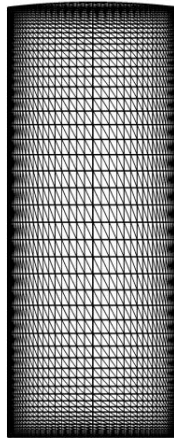
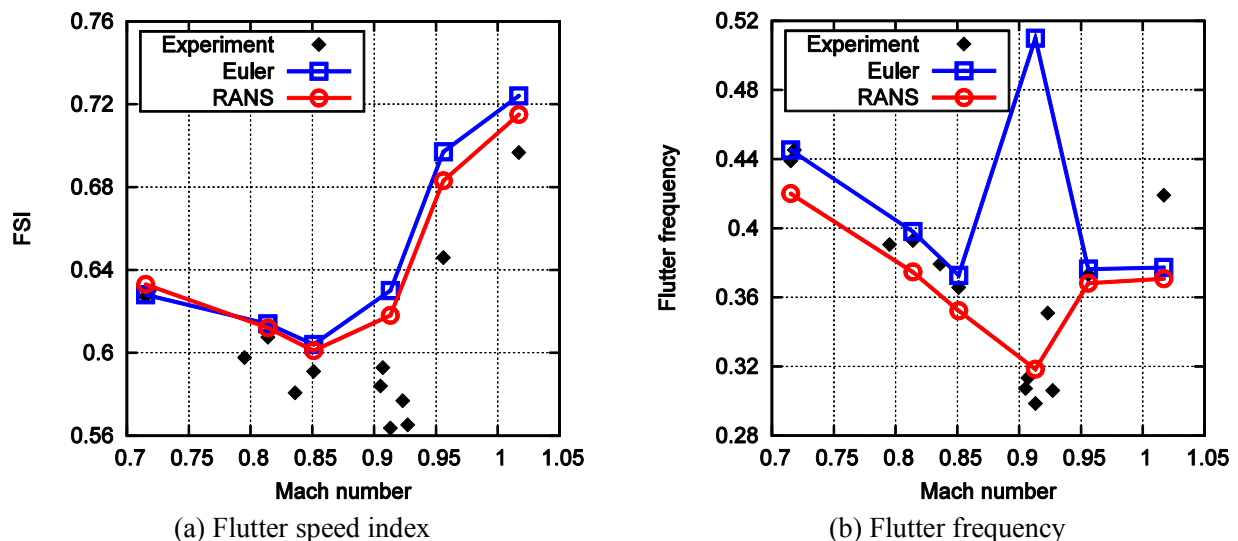Figure 10: Surface mesh in Euler and RANS computations for the rectangular wing.

(a) Flutter speed index   (b) Flutter frequency

Figure 11: Flutter boundary values for the rectangular wing.

4. CONCLUSIONS

Two flutter cases are computed using the present aeroelastic code based on the spectral volume discretization for aerodynamic analysis and on the modal structure analysis. In the AGARD 445.6 wing flutter case, the transonic dip is well reproduced. Considering viscous effects improve the flutter boundary values at the supersonic freestream regime. In the rectangular wing flutter case, the transonic dip in the FSI boundaries cannot reproduced well. Accounting for viscous effects does not improve significantly the FSI boundary values in high Mach number condition but improve particularly the flutter frequency.

REFERENCES

1) Nakamichi, J., "Coupling Dynamics in Flutter Analysis," *Japan Computational Fluid Dynamics Journal*, Vol. 9, No. 4, pp. 116–121, 2001.
2) Rodden, W. P., Taylor, P. F., and McIntosh, S. C., "Improvement to the Doublet-Lattice Method in MSC/NASTRAN."
3) Arizono, H. and Nakamichi, J., "Transonic Flutter Wind Tunnel Tests and Simulations for Twin-Jet Commercial Aircraft," *Japan Computational Fluid Dynamics Journal*, Vol. 26, No. 4, pp. 267–272, 2007.
4) Morino, H., "Multi-Objective Design Exploration and Aeroelastic Analysis for Next-Generation Regional

Jet Development," PhD thesis, Tohoku University, 2013.

5) Cockburn, B., "Discontinuous Galerkin Methods," *School of Mathematics*, pp. 1–25, 2003.

6) Wang, Z. J., "Spectral (finite) volume method for conservation laws on unstructured grids: Basic formulation," *Journal Computational Physics*, Vol. 178, No. 1, pp. 210–251, 2002.

7) Huynh, H. T., "A flux reconstruction approach to high-order schemes including discontinuous Galerkin methods," AIAA paper 2007-4079, 2007.

8) Wang, Z. J., Zhang, L., and Liu, Y., "Spectral (finite) volume method for conservation laws on unstructured grids IV: Extension to two-dimensional systems," *Journal Computational Physics*, Vol. 194, No. 2, pp. 716–741, 2004.

9) Sawaki, Y., Haga, T., Ogino, Y., Kawai, S., and Sawada, K., "Improved Spectral Volume Method (SV$^+$ Method) for Hybrid Unstructured Mesh," AIAA paper 2016-1327, 2016.

10) Mavriplis, D. J., and Yang, Z., "Achieving Higher-order Time Accuracy for Dynamic Unstructured Mesh Fluid Flow Simulations: Role of the GCL," AIAA paper 2005-5114, 2005.

11) Liu, Y., Vinokur, M., and Wang, Z. J., "Spectral (finite) volume method for conservation laws on unstructured grids V: Extension to three-dimensional systems," *Journal Computational Physics*, Vol. 212, No. 2, pp. 454–472, 2006.

12) Shima, E. and Kitamura, K., "On New Simple Low-Dissipation Scheme of AUSM-Family for All Speeds," AIAA paper 2009-136, 2009.

13) Sawaki, Y., Haga, T., Ogino, Y., and Sawada, K., "Wing Flutter Computation Using Modified Spectral Volume Method for Hybrid Unstructured Mesh," AIAA paper 2015-0768, 2015.

14) Bassi, F. and Rebay, S., "GMRES discontinuous Galerkin solution of the compressible Navier-Stokes equations," In *Discontinuous Galerkin Methods*, pp. 197–208, Springer, 2000.

15) Jameson, A. and Yoon, S., "Lower-upper implicit scheme with multiple grids for the Euler equations," *AIAA Journal*, Vol. 25, No. 7, pp. 929–935, 1987.

16) Yates, E. C. Jr., "AGARD Standard Aeloelastic Configuration for Dynamic Response I—Wing 445.6," NASA TM 100492, 1987.

17) Spalart, P. R. and Allmaras, S. R., "A one-equation turbulence model for aerodynamic flows," *La Recherche Aerospatiale*, Vol. 1, pp. 5–21, 1994.

18) Gan, J.-y., Im, H.-S., Chen, X.-y., Zha, G.-C., and Pasiliao, C. L., "Prediction of Wing Flutter Boundary Using High Fidelity Delayed Detached Eddy Simulation," AIAA paper 2015-0442, 2015.

19) Doggett, R. V. Jr., Rainey, A. G., and Morgan, H. G., "An Experimental Investigation of Aerodynamic Effects of Airfoil Thickness on Transonic Flutter Characteristics," NASA TM X-79, Technical report, 1959.